High-accuracy determination of the dependence of the photoluminescence emission energy on alloy composition in $Al_xGa_{1-x}As$ films

Lawrence H. Robins,[a] John T. Armstrong, Ryna B. Marinenko, Albert J. Paul, and Joseph G. Pellegrino[b]
National Institute of Standards and Technology, Gaithersburg, Maryland 20899

Kristine A. Bertness
National Institute of Standards and Technology, Boulder, Colorado 80305

(Received 19 August 2002; accepted 8 January 2003)

In an effort to improve the accuracy of photoluminescence (PL) measurements of the Al mole fraction ($\mathbf{x}$) of $Al_xGa_{1-x}As$ alloys, the PL peak emission energy, $\mathbf{E}_{PL,peak}$, was measured at room temperature for molecular-beam epitaxy-grown $Al_xGa_{1-x}As$ films with $0 \leqslant \mathbf{x} < 0.37$, and correlated with independent measurements of $\mathbf{x}$ by *in situ* reflective high-energy electron diffraction (RHEED) and also by *ex situ* wavelength-dispersive x-ray spectroscopy in an electron microprobe analyzer (WDS/EMPA). The measurement uncertainty of $\mathbf{E}_{PL,peak}$ was minimized through the following procedures: Accurate calibration of the photon energy (or wavelength) scale, correction of the measured spectra for the spectrometer response function, fitting the data with a well-chosen line shape function, and compensation for the effect of ambient temperature drift. With these procedures, the 2σ measurement uncertainty of $\mathbf{E}_{PL,peak}$ was of the order 5×10^{-4} eV for most samples. From correlation of the PL and WDS/EMPA composition data, the slope $\partial\mathbf{E}_{PL,peak}/\partial\mathbf{x}$ near room temperature was determined to be $\partial\mathbf{E}_{PL,peak}/\partial\mathbf{x} = (1.4017\pm0.0090\ \text{eV}) - [(2.71\pm0.97)\times10^{-4}\ \text{eV/K}](\mathbf{T}-298.3\ \text{K})$. Correlation with the RHEED data gave the same result within measurement uncertainty. Previously published measurements of $\partial\mathbf{E}_{PL,peak}/\partial\mathbf{x}$ were reviewed and compared with the present study. The results of T. F. Kuech *et al.* [Appl. Phys. Lett. **51**, 505 (1987)], based on nuclear resonant reaction analysis of the Al mole fraction, were found to be in good agreement with the present study after the addition of a correction term to account for the sample temperature difference ($\mathbf{T}=2$ K for Kuech *et al.*, $\mathbf{T}=298$ K for the present study).
[DOI: 10.1063/1.1556554]

I. INTRODUCTION

Chemical composition is one of the most fundamental material properties of an alloy crystal with continuously variable composition, and one of the most difficult to measure. Accurate measurement methods for the composition of III–V semiconductor alloys, e.g., the Al mole fraction $\mathbf{x}$ in $Al_xGa_{1-x}As$, or In fraction $\mathbf{x}$ and As fraction $\mathbf{y}$ in $In_xGa_{1-x}As_yP_{1-y}$, offer significant practical benefits, such as facilitating the exchange of wafers grown by different laboratories, and providing more accurate input parameters for device simulations. The desired level of accuracy (absolute uncertainty of $\mathbf{x}$) depends on the intended application of the data, and is usually stated to be in the range ±0.001 to ±0.005.

Photoluminescence (PL) spectroscopy is commonly used to estimate the composition of compound semiconductor alloys, based on the linear (or, in some systems, quadratic) composition dependence of the band-edge luminescence emission energy. PL spectroscopy, as well as other spectroscopic methods such as photoreflectance, does not directly measure the major-element atomic concentrations. Rather, the PL energy is a function of the alloy composition, but is also influenced by factors extraneous to major-element composition, such as temperature, strain, and donor and acceptor impurities. Thus, PL is described as an indirect (or nonself-calibrating) composition measurement method. Accurate PL-based composition measurements become possible when the PL results are correlated with direct (or self-calibrating) composition measurements.

The primary goals of the present study are to minimize the measurement uncertainty of the PL peak energy, $\mathbf{E}_{PL,peak}$, of $Al_xGa_{1-x}As$ films, to minimize any shifts in $\mathbf{E}_{PL,peak}$ caused by extraneous factors (other than Al mole fraction), and to accurately determine the functional dependence of $\mathbf{E}_{PL,peak}$ on Al mole fraction $\mathbf{x}$ in the direct gap composition range ($0\leqslant\mathbf{x}\leqslant0.37$). (Note that $\mathbf{E}_{PL,peak}$ is defined as the energy at which the emitted PL intensity is maximum.) Achieving these goals will enable accurate PL-based composition measurements, i.e., quantitative determination of $\mathbf{x}$ from $\mathbf{E}_{PL,peak}$. This study was performed as part of an ongoing effort to develop $Al_xGa_{1-x}As$ films for composition standards within the Standard Reference Materials (SRM) Program[1] at the National Institute of Standards and Technology (NIST).

More specifically, a set of 21 molecular-beam epitaxy (MBE)-grown $Al_xGa_{1-x}As$ films on GaAs substrates, with compositions between $\mathbf{x}=0$ and $\mathbf{x}=0.37$ and film thickness

[a]Electronic mail: lawrence.robins@nist.gov
[b]Currently at BAE Systems, Merrimack, NH 03054.

Downloaded 17 Feb 2005 to 132.163.53.137. Redistribution subject to AIP license or copyright, see http://jap.aip.org/jap/copyright.jsp

of 3 μm, was examined by three characterization techniques: First, *in situ* reflection high-energy electron diffraction (RHEED) measurements of the atomic growth rates during the deposition process; second, *ex situ* measurements of the Al, Ga, and As concentrations by wavelength-dispersive x-ray spectroscopy in an electron microprobe analyzer (WDS/EMPA); and third, room-temperature PL. Both RHEED and WDS/EMPA are, in principle, direct measurement methods for **x**. However, systematic errors may arise from the measurement, data reduction, and analysis procedures.

There have been a number of previous studies[2–10] of the dependence of the band gap energy ($\mathbf{E}_G$) of $Al_xGa_{1-x}As$, measured by PL or other optical techniques, on **x**, measured by methods such as WDS/EMPA, energy dispersive x-ray spectroscopy electron microprobe analysis (EDS/EMPA), or nuclear resonant reaction analysis (NRRA). The results of the previous studies differ significantly from each other. Measurements of **x** are more susceptible to systematic error than measurements of $\mathbf{E}_G$, thus we attribute the inconsistency of the published results primarily to systematic error in the reported **x** values. We believe that our study is the most accurate for the following reasons. First, a larger sample set was examined than in any single previous study. Second, the composition of each sample was determined independently by two direct methods, RHEED and WDS. The root mean squared (rms) difference between these two composition determinations within the sample set was $\Delta\mathbf{x}=0.0040$, and the maximum difference was $\Delta\mathbf{x}=0.0099$. Third, efforts were made to understand and minimize the systematic errors in each measurement (**x** by RHEED and WDS, optical band gap by PL).

II. EXPERIMENTAL PROCEDURE

PL measurements were performed on 21 $Al_xGa_{1-x}As$ films, thickness ≈ 3 μm, grown on (001)-oriented GaAs wafers in either of two MBE reactors, designated as reactor "A" and reactor "B." Four films were grown in reactor A and seventeen films were grown in reactor B. The initial wafer diameter during deposition was 5.0 cm to 5.2 cm. The Al mole fraction in each film was estimated by *in situ* RHEED measurements of the Al and Ga atomic fluxes. Some of the samples were made *n*-type or *p*-type conducting by doping with Si or Be. The room-temperature carrier concentrations of the samples were determined by capacitance–voltage measurements (reactor B) or estimated from a calibration curve of Si concentration in the film versus Si cell temperature during deposition[11] (reactor A). Both of these methods are expected to give the carrier concentration with an expanded uncertainty of $<10\%$. Four 10 mm$\times$10 mm pieces were diced from the central portion of each wafer. One piece from each wafer was characterized by room-temperature PL; a second piece was characterized by WDS/EMPA; and the remaining pieces were kept for other characterizations. Thus, for each wafer, the Al mole fraction, **x**, was measured by *in situ* RHEED and, independently, by *ex situ* WDS.

The excitation source for the PL-composition calibration measurements was a continuous wave Ar^+ laser operating at 2.54 eV (488.0 nm) and 0.0501 W incident power. The laser was focused by a cylindrical lens to an elliptical spot with a large height-to-width ratio. Because the monochromator entrance slit also has a large height-to-width ratio, the cylindrical lens provided higher throughput at a given intensity than could be attained with a spherical lens. The focused elliptical spot was measured to be 0.5 cm high$\times$0.008 cm wide. (The spot boundary is defined as the set of points where the local intensity is equal to $1/e^2$ of the peak intensity; a Gaussian beam profile is assumed.) At 0.0501 W incident power, the peak incident intensity was thus 41 W/cm^2. (The peak intensity, $\mathbf{I}_{peak}$, is given by the equation $\mathbf{I}_{peak}=(8/\pi)(\mathbf{P}/\mathbf{A})$ where **P** is the total power and **A** is the area of the ellipse.)

The PL was focused onto the monochromator entrance slit by achromatic lenses; the scattered laser light was rejected by a long-pass filter. The monochromator focal length was 0.6 m; the entrance slit width was set to 0.005 cm or, for the samples with the weakest PL, 0.01 cm. The PL was detected by a photodiode array detector interfaced to a personal computer. The wavelength resolution was estimated to be 0.40 nm for 0.005 cm entrance slit width, and 0.55 nm for 0.01 cm slit width. The energy resolution at 0.005 cm slit width is 0.6 meV at 1.4 eV, and 1.2 meV at 1.95 eV.

The photon energy (or wavelength) scale, i.e., the actual photon energy as a function of monochromator wavelength setting and detector pixel number, was calibrated with the spectral lines of neon and krypton vapor lamps. The atomic spectral line wavelengths are known to at least six decimal places. The wavelength calibration procedure was repeated at the beginning and end of each data collection run, to minimize any wavelength drift. With this procedure, the wavelength measurement uncertainty is estimated to be ± 0.05 nm, corresponding to a photon energy uncertainty of ± 0.08 meV at 1.4 eV, or ± 0.15 meV at 1.95 eV [note that all measurement uncertainties stated in this work are expanded (2σ) uncertainties, or equivalently 95% confidence intervals]. In addition, the measured PL spectra were corrected by dividing by the spectrometer response function, which was measured with a 100 W tungsten–halogen lamp that had previously been calibrated against a NIST standard irradiance source.

After the calibration and correction procedures were applied, the PL spectra were analyzed by the curve fitting of a model line shape function to the data. The selected model function yields a good fit with a small number of adjustable parameters, as described in the Appendix. The primary purpose for the curve fitting was to quantify $\mathbf{E}_{PL,peak}$, but other parameters, such as the full width at half maximum, integrated PL intensity, and asymmetry (skewing), can also be extracted from the fit.

Sample temperature is one of the extraneous factors that affects $\mathbf{E}_{PL,peak}$. For 14 of the 21 samples, the temperature coefficient of $\mathbf{E}_{PL,peak}$ was measured by recording PL spectra at temperatures between ambient (room) temperature and ≈ 40 K above ambient. The sample temperature was monitored with a miniature platinum resistive sensor. The sample was attached to an aluminum mounting block with a thermally conducting adhesive (Dow-Corning 340 silicone heat sink compound)[12] and the temperature sensor was attached to

Downloaded 17 Feb 2005 to 132.163.53.137. Redistribution subject to AIP license or copyright, see http://jap.aip.org/jap/copyright.jsp

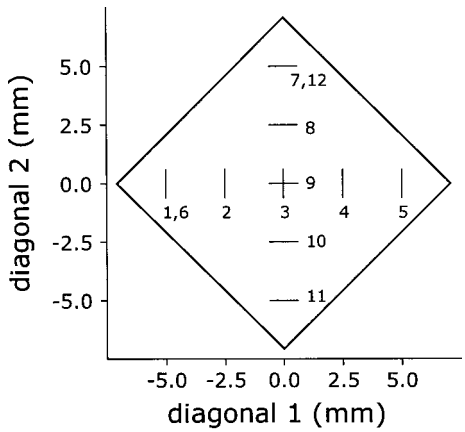

FIG. 1. Schematic of standard 12-location pattern used to examine spatial variation of PL spectrum on surface of 10 mm×10 mm sample. For each location, the laser-excited region is shown as a vertical or horizontal line segment, which approximates the focused laser spot geometry (high aspect ratio).

the block, near the sample, with graphite paste. The temperature sensor controller[12] (Omega Engineering CN9000A) provided a built-in calibration curve, which was recalibrated at 273.15 K by immersion of the sensor in an ice–water bath; the built-in calibration curve was assumed to be accurate after the one-point recalibration. For the elevated-temperature measurements, heater coils were placed around the sample mounting block. Each time the heater current was changed, a time interval of 30 to 45 min was allowed for the temperature to reach a steady-state value before starting the PL data acquisition (approximately 1 min duration).

The ambient temperature in our setup was controlled only by the building heating and cooling system; ambient temperature variations (from the long-term average of ≈24 °C) were as large as ±2 K. To measure and thus correct for the effect of ambient temperature variation, the sample temperature monitored by the platinum resistive sensor was recorded for each ''room-temperature'' PL spectrum.

Another experiment was done to measure sample heating by the laser beam. In this experiment, a set of sixteen PL spectra were acquired from one sample, with laser power alternating between the standard power of 0.0501 W (peak intensity=41 W/cm^2), and a lower power of 0.0157 W (peak intensity=13 W/cm^2) for consecutive spectra. If the temperature coefficient of $\mathbf{E}_{\mathrm{PL,peak}}$ is known, then the shift of $\mathbf{E}_{\mathrm{PL,peak}}$ with excitation power can be equated to a laser-induced temperature rise.

Samples were examined for possible spatial variation of $\mathbf{E}_{\mathrm{PL,peak}}$ by recording spectra from several discrete locations on the specimen surface. A ''criss-cross'' pattern of twelve PL measurements from ten locations (included repeated measurements of two locations) was defined to standardize sample-to-sample comparison of the spatial variation. The test pattern for spatial variation is illustrated in Fig. 1.

III. RESULTS AND DISCUSSION

A. Photoluminescence line shape

Representative PL spectra of four samples are shown in Fig. 2(a). The PL spectrum of each sample consists of a single asymmetric bell-shaped peak skewed toward high energy (i.e., the high-energy tail is broader than the low-energy tail). $\mathbf{E}_{\mathrm{PL,peak}}$ increases with increasing Al fraction, as reported previously.[2–10] Figure 2(b) shows a representative PL spectrum of sample B217, with $\mathbf{x}_{\mathrm{WDS}}=0.3057$, as well as the fitted model function. An inset to Fig. 2(b) shows the same data and fitted function plotted on a semilogarithmic scale. It can be seen that both the high-energy and low-energy tails have exponential forms. This is important for the selection of the model function, as discussed in the Appendix.

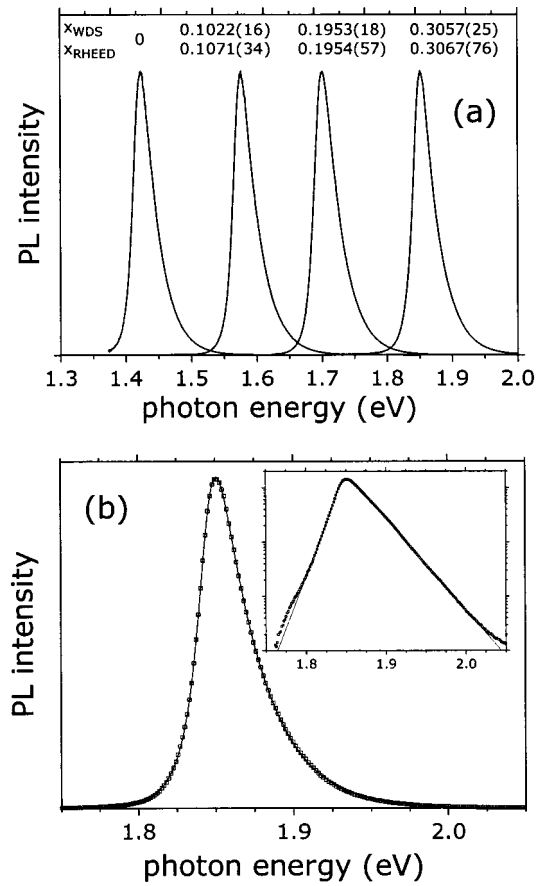

FIG. 2. (a) Room-temperature PL spectra of a GaAs homoepitaxial film ($\mathbf{x}=0$) and three $\mathrm{Al}_x\mathrm{Ga}_{1-x}\mathrm{As}$ films with differing compositions, acquired with excitation photon energy=2.54 eV, excitation intensity=41 W/cm^2, and sample temperature ≈298 K. The Al mole fractions measured by RHEED and WDS, $\mathbf{x}_{\mathrm{RHEED}}$ and $\mathbf{x}_{\mathrm{WDS}}$, are shown. The measurement uncertainties of $\mathbf{x}_{\mathrm{RHEED}}$ and $\mathbf{x}_{\mathrm{WDS}}$ (least significant digits) are shown in parentheses. (b) Room-temperature PL spectrum of $\mathrm{Al}_x\mathrm{Ga}_{1-x}\mathrm{As}$ film B217 with $\mathbf{x}_{\mathrm{WDS}}=0.3057$. Experimental data are shown as open squares, fitted model function is shown as a solid line. Only every fourth data point is plotted to improve visibility. The data and fit are replotted on a semilogarithmic scale in the inset.

B. Temperature dependence

The temperature dependence of $\mathbf{E}_{\mathrm{PL,peak}}$ for sample B217, and the best linear fit $\mathbf{E}_{\mathrm{PL,peak}}[\mathbf{T}]$, are plotted in Fig. 3. (Error bars are not shown in Fig. 3 because the measurement uncertainty of $\mathbf{E}_{\mathrm{PL,peak}}[\mathbf{T}]$ is small compared to the vertical scale.) The slope of the fitted line, which gives the temperature coefficient of $\mathbf{E}_{\mathrm{PL,peak}}[\mathbf{T}]$ near room temperature, will be denoted $\mathbf{E}'_{T0}$. By examining the variation of $\mathbf{E}'_{T0}$ for samples with different $\mathbf{x}$ values and carrier concentrations ($\mathbf{n}$), an em-

Downloaded 17 Feb 2005 to 132.163.53.137. Redistribution subject to AIP license or copyright, see http://jap.aip.org/jap/copyright.jsp

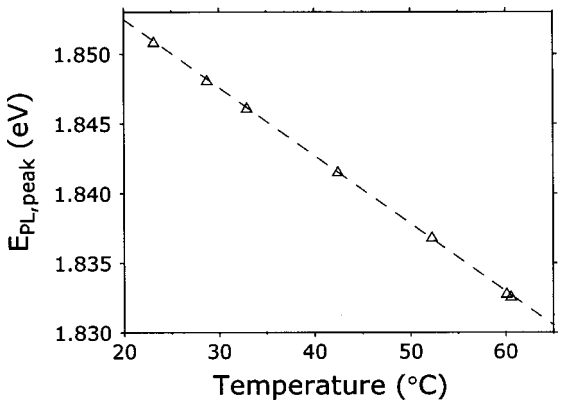

FIG. 3. Temperature dependence of $\mathbf{E}_{\mathrm{PL,peak}}$ for sample B217. Data are shown as open triangles, best linear fit is shown as a dashed line. The uncertainty of $\mathbf{E}_{\mathrm{PL,peak}}$ for these measurements is of the order 1.5×10^{-4} eV; error bars are not shown because of the small magnitude of the uncertainties relative to the plot scale.

pirical equation was derived for the dependence of $\mathbf{E}'_{T0}$ on $\mathbf{x}$ and $\mathbf{n}$ (where $\mathbf{n}$ is taken to be a signed quantity, positive for holes, negative for electrons):

$$\mathbf{E}'_{T0}(\mathrm{eV/K}) = -(4.74\pm0.23)\times10^{-4} - (2.71\pm0.97)\times10^{-4}\mathbf{x} + ((1.05\pm0.16)\times10^{-10} - (0.29\pm0.11)\times10^{-10}\,\mathrm{sgn}[\mathbf{n}])|\mathbf{n}|^{1/3}. \quad (1)$$

(A comment on mathematical notation: Square brackets [ ] are used to indicate functional dependence, e.g., sgn[$\mathbf{n}$], $\mathbf{E}_{\mathrm{PL,peak}}[\mathbf{T}]$.) To better display the variation of $\mathbf{E}'_{T0}[\mathbf{x},\mathbf{n}]$ with $\mathbf{x}$ and with $\mathbf{n}$, two additional functions are defined, $\mathbf{G}'_{T0}[\mathbf{x}]$ and $\mathbf{H}'_{T0}[\mathbf{n}]$, where $\mathbf{G}'_{T0}$ is obtained by subtracting the $\mathbf{n}$-dependent terms from $\mathbf{E}'_{T0}[\mathbf{x},\mathbf{n}]$, and $\mathbf{H}'_{T0}[\mathbf{n}]$ is obtained by subtracting the $\mathbf{x}$-dependent terms. The function definitions are

$$\mathbf{G}'_{T0}[\mathbf{x}] = \mathbf{E}'_{T0} - (1.05\times10^{-10} - 0.29\times10^{-10}\,\mathrm{sgn}[\mathbf{n}])|\mathbf{n}|^{1/3}, \quad (2)$$

$$\mathbf{H}'_{T0}[\mathbf{n}] = \mathbf{E}'_{T0} + 2.71\times10^{-4}\mathbf{x}. \quad (3)$$

$\mathbf{G}'_{T0}[\mathbf{x}]$ is plotted against $\mathbf{x}$ in Fig. 4(a), and $\mathbf{H}'_{T0}[\mathbf{n}]$ is plotted against sgn[$\mathbf{n}$]$|\mathbf{n}|^{1/3}$ in Fig. 4(b).

Previously, Lautenschlager *et al.*[13] and Logothetidis *et al.*[14] did a detailed study of the temperature dependence of the direct band gap and other critical point energies in GaAs and in three $\mathrm{Al}_x\mathrm{Ga}_{1-x}\mathrm{As}$ films with nominal compositions (determined from "x-ray studies and from E_0 and E_1 energy gaps at room temperature") of $\mathbf{x}=0.27$, $\mathbf{x}=0.53$, and $\mathbf{x}=0.69$. Equation (4) for the temperature coefficient of the direct band gap near room temperature was derived from the functional results of Lautenschlager *et al.*[13] and Logothetidis *et al.*:[14]

$$\mathbf{E}'_{T0}(\mathrm{eV/K}) = -4.60\times10^{-4} - 2.36\times10^{-4}\mathbf{x}. \quad (4)$$

If the carrier-concentration-dependent term in Eq. (1) (not considered by Lautenschlager *et al.*[13] or Logothetidis *et al.*[14]) is neglected, then Eqs. (4) and (1) are seen to agree within the measurement uncertainty of Eq. (1). Our result,

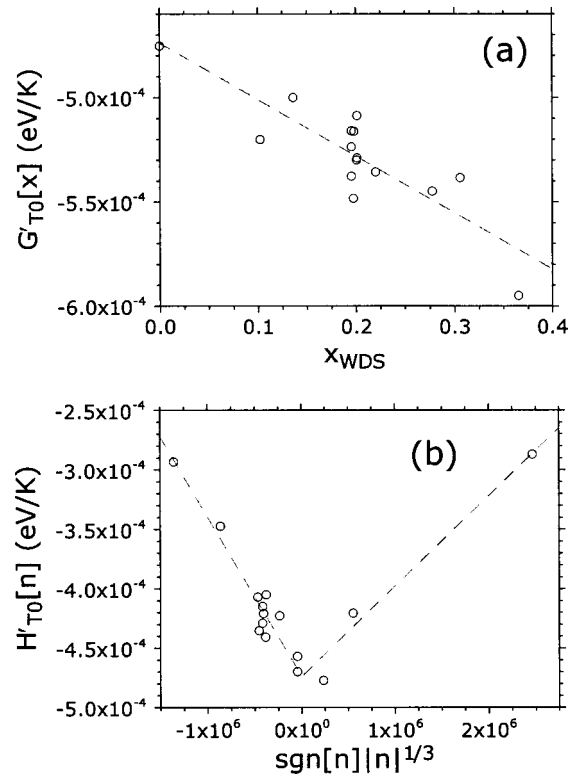

FIG. 4. (a) Temperature coefficient of $\mathbf{E}_{\mathrm{PL,peak}}$ with $\mathbf{n}$-dependent term subtracted, $\mathbf{G}'_{T0}[\mathbf{x}]=\mathbf{E}'_{T0}-(1.05\times10^{-10}-0.29\times10^{-10}\,\mathrm{sgn}[\mathbf{n}])|\mathbf{n}|^{1/3}$, plotted as function of Al fraction $\mathbf{x}$. Data are shown as open circles, best linear fit is shown as a dashed line. (b) Temperature coefficient of $\mathbf{E}_{\mathrm{PL,peak}}$ with $\mathbf{x}$-dependent term subtracted, $\mathbf{H}'_{T0}[\mathbf{n}]=\mathbf{E}'_{T0}+2.71\times10^{-4}\,\mathbf{x}$, plotted as a function of sgn[$\mathbf{n}$]$|\mathbf{n}|^{1/3}$ where $\mathbf{n}$ is the carrier concentration. Data are shown as open circles, best fit is shown as a dashed line.

Eq. (1), is probably more accurate than Eq. (4) because of the larger sample set (14 rather than 4 samples) and the higher accuracy of the composition ($\mathbf{x}$) measurements.

C. Laser heating effect

The results of the laser beam heating measurement with alternating high and low excitation intensities, for sample B395 with $\mathbf{x}_{\mathrm{WDS}}=0.365$, are displayed in Fig. 5. $\mathbf{E}_{\mathrm{PL,peak}}$ values for the eight measurements at the higher peak intensity (41 W/cm^2) are plotted as open squares, and $\mathbf{E}_{\mathrm{PL,peak}}$ values for the eight measurements at the lower peak intensity (13 W/cm^2) are plotted as open triangles in Fig. 5. The average values of $\mathbf{E}_{\mathrm{PL,peak}}$ at the higher and lower intensity are shown as a dashed line and a dashed–dotted line, respectively. From the peak shift of -4.3×10^{-4} eV on going from the lower to the higher intensity, and the fitted temperature coefficient of -5.25×10^{-4} eV/K for this sample, the calculated temperature rise within the laser-excited region is 0.82 K, as indicated by the downward-pointing arrow in Fig. 5. If the temperature is assumed to increase linearly with excitation intensity, then the temperature rise from zero intensity to 13 W/cm^2 is calculated to be 0.38 K, as indicated by the downward-pointing dashed arrow in Fig. 5. Further, the total temperature rise from zero intensity to 41 W/cm^2 is calculated to be 1.2 K. For the samples with the largest temperature coefficient, $\mathbf{E}'_{T0}=-5.3\times10^{-4}$ eV/K, this temperature

Downloaded 17 Feb 2005 to 132.163.53.137. Redistribution subject to AIP license or copyright, see http://jap.aip.org/jap/copyright.jsp

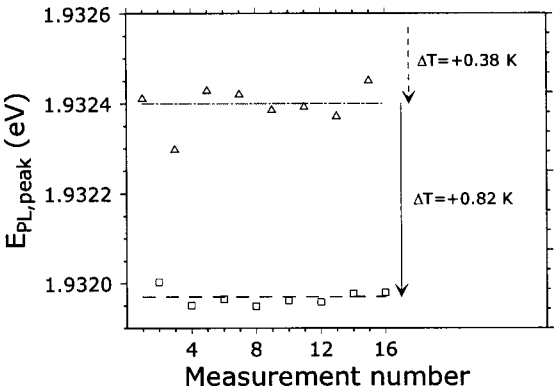

FIG. 5. Test of laser beam heating with alternating lower and higher excitation intensity, for sample B395 with $\mathbf{x}_{WDS}=0.365$. A total of sixteen PL spectra were acquired, eight spectra at peak intensity of 13 W/cm^2 (measurements 1, 3, ..., 15) and eight spectra at peak intensity of 41 W/cm^2 (measurements 2, 4, ..., 16). (The peak intensity is the intensity at the center of the focused laser spot.) Individual $\mathbf{E}_{PL,peak}$ values measured at the lower and higher power are shown as open triangles and open squares, respectively; the average $\mathbf{E}_{PL,peak}$ values measured at the lower and higher power are shown as dashed–dotted and dashed lines, respectively. The calculated increases in sample temperature from zero intensity to 13 W/cm^2, and from 13 W/cm^2 to 41 W/cm^2, are also shown (vertical arrows).

rise would correspond to a shift in $\mathbf{E}_{PL,peak}$ of -6.4×10^{-4} eV. Note that the laser-induced heating was not detected by the platinum resistive temperature sensor, which was mounted near the sample but not illuminated by the laser beam.

The higher excitation intensity of 41 W/cm^2 was selected as the standard excitation intensity for the PL composition measurements. In principle, it would be preferable to run at a lower intensity, in order to reduce the laser heating effect and associated temperature gradients in the sample. However, the 41 W/cm^2 setting was necessary to get data with good signal-to-noise from the samples with the lowest carrier concentration and lowest PL efficiency. The magnitude of the laser-induced heating effect at the standard excitation intensity is expected to be similar for all samples (provided that all samples have similar thermal properties).

D. Correction for ambient temperature fluctuations

As just pointed out, the ambient temperature varied by up to ±2 K. For the samples with the largest temperature coefficient, $\mathbf{E}'_{T0}=-5.3\times10^{-4}$ eV/K, temperature fluctuations of this magnitude would cause $\mathbf{E}_{PL,peak}$ to vary by $\pm1.1\times10^{-3}$ eV. A simple procedure was developed to compensate for the ambient temperature fluctuations. First, the ambient temperature read by the platinum resistive sensor, denoted $\mathbf{T}_{sensor}$, was recorded for each PL measurement. Second, the standard ambient temperature was defined to be $\mathbf{T}_{a,std}=24\,°C$ (similar to the long-term average). Third, the calculated temperature coefficient of each sample, $\mathbf{E}'_{T0}$ from Eq. (1), was used to transform $\mathbf{E}_{PL,peak}$ from the measured value at the measured ambient temperature $\mathbf{T}_{sensor}$ (where $\mathbf{T}_{sensor}$ may be different for each PL measurement) to the predicted value at the standard temperature $\mathbf{T}_{a,std}$. The equation for this transformation is

$$\mathbf{E}_{PL,peak}[\mathbf{T}_{a,std}]=\mathbf{E}_{PL,peak}[\mathbf{T}_{sensor}]-\mathbf{E}'_{T0}[\mathbf{x},\mathbf{n}](\mathbf{T}_{sensor}-\mathbf{T}_{a,std}). \quad (5)$$

From here on, unless otherwise noted, the reported values of $\mathbf{E}_{PL,peak}$ will be assumed to be the temperature-compensated values from Eq. (5). As just pointed out, at the standard excitation intensity, the temperature of the laser-excited sample volume, denoted $\mathbf{T}_{exc}$, is estimated to be 1.2 K higher than ambient. Thus, at $\mathbf{T}_{a,std}=24\,°C$, the temperature of the laser-excited volume is $\mathbf{T}_{exc}=25.2\,°C=298.3$ K.

Any errors in the ambient temperature measurements will give rise to errors in the temperature-compensation procedure. From Eq. (5), an uncertainty of $2\sigma_{T,sensor}$ in the temperature correction term $(\mathbf{T}_{sensor}-\mathbf{T}_{a,std})$ will contribute a factor $(\mathbf{E}'_{T0}[\mathbf{x},\mathbf{n}])(2\sigma_{T,sensor})$ to the overall measurement uncertainty of $\mathbf{E}_{PL,peak}[\mathbf{T}_{a,std}]$. A procedure for estimating the magnitude of this contribution to the uncertainty is discussed in Sec. III E.

E. Calculation of the average value and uncertainty of $\mathbf{E}_{PL,peak}$ for each sample

The ambient-temperature PL measurements were performed within a 16 month period. For some samples, all the spectra were acquired in a single run (on one day), while for other samples, spectra were acquired in multiple runs (different days within the 16 month period). Between 5 and 42 spectra were recorded for each sample, with a minimum of 5 spectra per run. Examination of the data shows that, for at least some samples, the long-term or ''run-to-run'' variation of $\mathbf{E}_{PL,peak}$ is larger than the short-term or ''intrarun'' variation. For samples with multiple runs, it was therefore decided to weight each run equally in calculating the long-term average and statistical uncertainty of $\mathbf{E}_{PL,peak}$, rather than weighting each individual spectrum equally, on the assumption that the data is best represented in a statistical sense by giving equal importance to each run.

For conciseness, the following notation will be used in discussing the calculation of the average value and uncertainty of $\mathbf{E}_{PL,peak}$. Each sample will be referred to by an index number s. The total number of runs for sample s will be denoted $K[s]$, and the index of an individual run will be denoted k (for sample s, the range of k is thus 1 to $K[s]$). The number of spectra acquired within a given run k will be denoted $J[k]$, and the index of an individual spectrum will be denoted j (for run k, the range of j is thus 1 to $J[k]$). The total number of spectra acquired for sample s in all runs will be denoted $N[s]\equiv\Sigma_{k=1,K[s]}J[k]$. Finally, the peak PL energy for sample s, run k, spectrum j will be denoted $\mathbf{E}_{PL,peak}[j,k,s]$.

With this notation, the average value of $\mathbf{E}_{PL,peak}$ for sample s, run k is

$$\mathbf{E}_{avg}[k,s]=(1/J[k])\Sigma_{j=1,J[k]}\mathbf{E}_{PL,peak}[j,k,s], \quad (6)$$

and, applying the assumption that each run should be equally weighted, the overall or long-term average value of $\mathbf{E}_{PL,peak}$ for sample s is

Downloaded 17 Feb 2005 to 132.163.53.137. Redistribution subject to AIP license or copyright, see http://jap.aip.org/jap/copyright.jsp

$$\mathbf{E}_{\text{long-term}}[s]=(1/K[s])\Sigma_{k=1,K[s]}\mathbf{E}_{\text{avg}}[k,s]$$
$$=\Sigma_{k=1,K[s]}\Sigma_{j=1,J[k]}$$
$$\{\mathbf{E}_{\text{PL,peak}}[j,k,s]/(J[k]K[s])\}. \quad (7)$$

It can be shown that the statistical uncertainty of $\mathbf{E}_{\text{long-term}}[s]$ (sample standard deviation from the mean) is

$$\sigma_{E,\text{stat}}[s]$$
$$=\{(N[s]/(N[s]-1))\Sigma_{k=1,K[s]}\Sigma_{j=1,J[k]}$$
$$(\mathbf{E}_{\text{PL,peak}}[j,k,s]-\mathbf{E}_{\text{long-term}}[s])^2/(J[k]K[s])\}^{0.5}. \quad (8)$$

(The effect of the prefactor $(N[s]/(N[s]-1)$ is to make $\sigma_{E,\text{stat}}[s]$ undetermined, rather than zero, if there is only one data point for sample s $(N[s]=1)$.)

In addition to $\sigma_{E,\text{stat}}[s]$, two other terms may contribute to the measurement uncertainty of $\mathbf{E}_{\text{long-term}}[s]$. As already measured, temperature measurement error will contribute a term $(\mathbf{E}'_{T0}[\mathbf{x},\mathbf{n}])(2\sigma_{T,\text{sensor}})$ to the overall measurement uncertainty, where $2\sigma_{T,\text{sensor}}$ is the uncertainty of the temperature correction term $(\mathbf{T}_{\text{sensor}}-\mathbf{T}_{a,\text{std}})$. The magnitude of this term is estimated by assuming that, for samples with data from multiple runs, the differences between the single-run averages of $\mathbf{E}_{\text{PL,peak}}$ [Eq. (6)] and the long-term average [Eq. (7)] arise primarily from the temperature-compensation error. In other words, it is assumed that there is a small error in the temperature sensor reading that varies on a long time scale (between runs). Comparison of the sensor readings with other temperature measurement devices supported this hypothesis. (Note that the possible contribution of spatial inhomogeneity to the run-to-run variation of $\mathbf{E}_{\text{avg}}[k,s]$ is neglected in this model. As discussed in Sec. III F, the spatial inhomogeneity effect is to small to explain the observed run-to-run variation of $\mathbf{E}_{\text{avg}}[k,s]$ for most samples.)

According to this above model, the magnitude of the temperature-compensation error for sample s, run k, is

$$\varepsilon_{T,\text{sensor}}[k,s]=(\mathbf{E}_{\text{avg}}[k,s]-\mathbf{E}_{\text{long-term}}[s])/\mathbf{E}'_{T0}[s], \quad (9)$$

where $\mathbf{E}'_{T0}[s]=\mathbf{E}'_{T0}[\mathbf{x}[s],\mathbf{n}[s]]$ is the temperature coefficient from Eq. (1). The calculated values of $\varepsilon_{T,\text{sensor}}[k,s]$, for four samples with data from at least three runs, are plotted in Fig. 6. The overall uncertainty $2\sigma_{T,\text{sensor}}$ is equated to twice the rms value of $\varepsilon_{T,\text{sensor}}[k,s]$; the calculated value, $2\sigma_{T,\text{sensor}}=0.62$ K, is shown in Fig. 6. For the samples with the largest temperature coefficient, $\mathbf{E}'_{T0}=-5.3\times10^{-4}$ eV/K, the measurement uncertainty of $\mathbf{E}_{\text{long-term}}[s]$ due to the temperature uncertainty is $\pm3.3\times10^{-4}$ eV. The corresponding uncertainty in the Al fraction determined from PL (as discussed next) is $\pm2.3\times10^{-4}$.

The final term known to contribute to the measurement uncertainty of $\mathbf{E}_{\text{long-term}}[s]$ is the wavelength scale uncertainty of 0.05 nm, which equates to a photon energy scale uncertainty of $(0.05/1239.5)\mathbf{E}_{\text{long-term}}{}^2[s]$. The wavelength uncertainty makes a negligibly small contribution compared to the other terms.

Adding the statistical uncertainty, temperature-compensation uncertainty, and wavelength uncertainty in quadrature, the total measurement uncertainty of $\mathbf{E}_{\text{long-term}}[s]$ is found to be

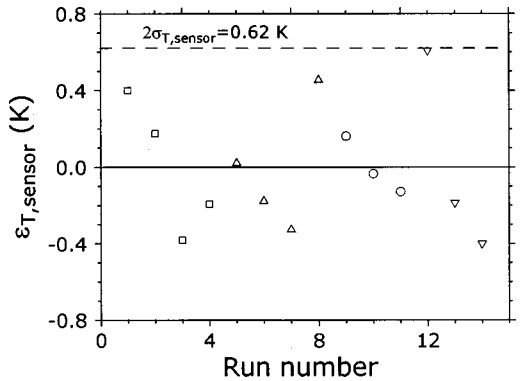

FIG. 6. Calculated temperature sensor errors for samples with $\mathbf{E}_{\text{PL,peak}}$ data from at least three different runs. The temperature error for each run is shown for samples B212 (squares), B215 (triangles), B309 (circles), and B395 (inverted triangles). The calculated uncertainty of the temperature sensor reading is shown as a dashed line ($2\sigma_{T,\text{sensor}}=0.62$ K).

$$2\sigma_{E,\text{long-term}}[s]=\{4\sigma^2_{E,\text{stat}}[s]+4\sigma^2_{T,\text{sensor}}\mathbf{E}'^2_{T0}[s]+1.63$$
$$\times10^{-9}\mathbf{E}^4_{\text{long-term}}[s]\}^{0.5}. \quad (10)$$

Note that for samples with data from several runs (Fig. 6), there is some "error double counting," because the temperature-compensation error, the second term in Eq. (10), also contributes to the observed ("statistical") variation of $\mathbf{E}_{\text{PL,peak}}[j,k,s]$, the first term in Eq. (10). The error double counting was found to increase $2\sigma_{E,\text{long-term}}[s]$ by no more than 10%; therefore, no effort was made to remove this effect. The calculated values of $2\sigma_{E,\text{long-term}}[s]$ (of the order 5×10^{-4} eV for most samples) are listed in Table I.

F. Mapping of spatial inhomogeneity

To assess the spatial variation of $\mathbf{E}_{\text{PL,peak}}$, measurements were taken from several different locations on the surface of each sample. The "standard spatial scan pattern" shown in Fig. 1 was used for most of the samples. A few samples suffered breakage before measurements could be done. For the broken samples, different spatial scan patterns were used than shown in Fig. 1. Note that, in the standard pattern, spot 6 matches spot 1 and spot 12 matches spot 7; also, the centers of spots 3 and 9 intersect. The positioning accuracy within each half of the scan, that is from spot 1 to spot 6 (repeat of 1), and from spot 7 to spot 12, is approximately 0.02 mm, determined by a micrometer-drive translation stage. However, because the sample was remounted on the holder between the measurement of spots 6 and 7, the accuracy of the beam positioning between the two halves of the scan was much lower; the distance between the centers of spots 3 and 9 (shown to intersect in Fig. 1) may be as high as 1 mm.

The spatial scan pattern results for two samples from reactor B, denoted B380 and B394, and two samples from reactor A, denoted A117 and A119, are plotted in Figs. 7(a)–7(d). This group of samples was selected to demonstrate that the magnitude of the inhomogeneity varies from sample to sample. Note that, in Fig. 7, a coordinate of 0 mm indicates the center of the sample, that is spot 3 for "diagonal 1," or spot 9 for "diagonal 2." Note also that the y-axis ($\mathbf{E}_{\text{PL,peak}}$)

Downloaded 17 Feb 2005 to 132.163.53.137. Redistribution subject to AIP license or copyright, see http://jap.aip.org/jap/copyright.jsp

TABLE I. Some important experimental and fitting parameters for the examined samples: Column 1, sample name; column 2, PL peak energy and measurement uncertainty $\mathbf{E}_{\mathrm{PL,peak}}[s]\pm 2\sigma_{\mathrm{E,total}}[s]$; column 3, WDS composition and measurement uncertainty, $\mathbf{x}_{\mathrm{WDS}}[s]\pm 2\sigma_1[s]$; column 4, RHEED composition and measurement uncertainty, $\mathbf{x}_{\mathrm{WDS}}[s]\pm 2\sigma_2[s]$; column 5, fitted {PL|WDS} composition and calculated uncertainty $\mathbf{x}_{\{\mathrm{PL|WDS}\}}[s]\pm 2\sigma_3[s]$; column 6, component of uncertainty of $\mathbf{x}_{\{\mathrm{PL|WDS}\}}$ that arises from PL energy uncertainty; column 7, component of uncertainty of $\mathbf{x}_{\{\mathrm{PL|WDS}\}}$ that arises from uncertainty of the slope $\partial\mathbf{x}_{\mathrm{WDS}}/\partial\mathbf{E}_{\mathrm{PL,peak}}$. Uncertainties are shown in the least significant digits, i.e., 1.423 26(47) is read as 1.423 26±0.000 47. It is assumed that $x=0$ exactly for sample B213. The first fifteen rows show the samples included in the PL-composition calibration set; the last six rows show the samples excluded from the calibration set. The WDS composition of sample A128 was not measured; the last three data columns for A128 are therefore based on $\mathbf{x}_{\{\mathrm{PL|RHEED}\}}$ rather than $\mathbf{x}_{\{\mathrm{PL|WDS}\}}$.

Sample	$\mathrm{E}_{\mathrm{PL,peak}}\pm 2\sigma_E$ (eV)	$\mathbf{x}_{\mathrm{WDS}}\pm 2\sigma_1$	$\mathbf{x}_{\mathrm{RHEED}}\pm 2\sigma_2$	$\mathbf{x}_{\{\mathrm{PL|WDS}\}}\pm 2\sigma_3$	$2\sigma_3$ (E_{PL} component)	$2\sigma_3$ (slope component)
B213	1.423 26(47)	0	0	0	NA[a]	NA[a]
B212	1.576 29(54)	0.1022(16)	0.1071(34)	0.1092(09)	0.000 51	0.000 70
B215	1.701 02(70)	0.1953(18)	0.1954(57)	0.1981(14)	0.000 60	0.001 27
B217	1.851 19(37)	0.3057(25)	0.3067(76)	0.3053(20)	0.000 43	0.001 96
B290	1.699 48(54)	0.1972(20)	0.1970(58)	0.1970(14)	0.000 51	0.001 27
B293	1.699 45(47)	0.1980(16)	0.1984(60)	0.1970(14)	0.000 47	0.001 27
B299	1.703 80(40)	0.1997(05)	0.1997(55)	0.2001(14)	0.000 44	0.001 29
B310	1.450 75(42)	0.0187(20)	0.0211(09)	0.0196(05)	0.000 45	0.000 13
B315	1.616 87(48)	0.1360(20)	0.1394(43)	0.1381(10)	0.000 47	0.000 89
B380	1.702 55(39)	0.2010(20)	0.1971(19)	0.1992(14)	0.000 43	0.001 28
B394	1.809 16(60)	0.2775(30)	0.2717(29)	0.2753(19)	0.000 54	0.001 77
B395	1.931 75(68)	0.3651(35)	0.3624(33)	0.3627(24)	0.000 59	0.002 33
B396	1.542 08(47)	0.0856(20)	0.0810(10)	0.0848(07)	0.000 47	0.000 54
A117	1.693 50(108)	0.1908(36)	0.2007(30)	0.1928(15)	0.000 84	0.001 24
A119	1.705 94(212)	0.2008(30)	0.2018(40)	0.2016(20)	0.001 55	0.001 29
B274	1.687 86(49)	0.2010(28)	0.1988(59)	0.1887(13)	0.000 48	0.001 21
B309	1.745 14(70)	0.2200(50)	0.2399(66)	0.2296(16)	0.000 60	0.001 47
B373	1.706 28(124)	0.1952(15)	0.2011(26)	0.2019(16)	0.000 95	0.001 30
B379	1.711 72(160)	0.2006(10)	0.1958(22)	0.2058(18)	0.001 19	0.001 32
A121	1.720 67(111)	0.2011(25)	0.2026(120)	0.2122(16)	0.000 86	0.001 36
A128	1.703 50(785)	NA[a]	0.1997(70)	0.1998(58)	0.005 61	0.001 51

[a]NA indicates not applicable.

range is different for each plot: 0.0006 eV in Fig. 7(a), 0.0012 eV in Fig. 7(b), 0.0022 eV in Fig. 7(c), and 0.0040 eV in Fig. 7(d).

The error bars on each data point in Fig. 7 represent a "fixed-location single-run" uncertainty, denoted $2\sigma_{\mathrm{fixed}}[s]$, which excludes spatial inhomogeneity, because that is the variable under examination in Fig. 7, and also excludes long-term or run-to-run drift. The magnitude of $2\sigma_{\mathrm{fixed}}[s]$ is smaller than $2\sigma_{E,\text{long-term}}[s]$, which includes inhomogeneity and long-term drift. From repeated fixed-location single-run measurements, $2\sigma_{\mathrm{fixed}}[s]$ is estimated to be 1.5×10^{-4} eV for most samples, including those examined in Fig. 7.

In Fig. 7, the samples are displayed in order of increasing inhomogeneity, from B380 to A119. As indicated by these results, samples from reactor A are generally more inhomogeneous than samples from reactor B. Sample A119 is the most inhomogeneous sample included in the PL-composition calibration set; for this sample, the largest observed spatial variation of the PL energy was $\Delta\mathbf{E}_{\mathrm{PL,peak}}=0.0033$ eV. With the calibration curve discussed next, this corresponds to a composition variation $\Delta\mathbf{x}=0.0023$. Note that, for samples B394, A117, and A119, the variation of $\mathbf{E}_{\mathrm{PL,peak}}$ for repeated measurements of the same location, that is spots 1/6 (squares at −5 mm) and spots 7/12 (triangles at −5 mm), is much smaller than the variation between different locations. This observation confirms that the spatial inhomogeneity effects are real, and not artifacts due to random measurement error.

In the context of composition SRM[1] development, the results of Fig. 7 indicate that PL spatial variation measurements may be used to select the more homogeneous wafers (with inhomogeneity below some arbitrary limit) from an initial set of wafers with varying amounts of inhomogeneity. Once an upper limit to the inhomogeneity of a particular wafer is established by PL, the wafer could be diced. Pieces of the original wafer could then be further analyzed by direct composition measurement methods, including destructive methods, with the knowledge that the Al mole fraction ($\mathbf{x}$) is the same for each piece within the established inhomogeneity limit.

Finally, it should be pointed out that the effect of spatial variation is already included in the calculation of $2\sigma_{E,\text{long-term}}[s]$ [Eq. (10)], because this calculation is based on measurements from different sample locations (the spatial scan patterns discussed here). Thus, the previous expression for $2\sigma_{E,\text{long-term}}[s]$ does not need to be modified.

G. Calibration curves for composition dependence of $\mathbf{E}_{\mathrm{PL,peak}}$

Of the total of 21 samples examined, 15 samples were included in the PL-composition calibration set (the pure GaAs film and 14 alloy films) and 6 were excluded. One of the A reactor samples (designated A128) and one of the B reactor samples (B309) were excluded for excessive inhomogeneity, as seen in the spatially resolved PL results (Fig. 7).

Downloaded 17 Feb 2005 to 132.163.53.137. Redistribution subject to AIP license or copyright, see http://jap.aip.org/jap/copyright.jsp

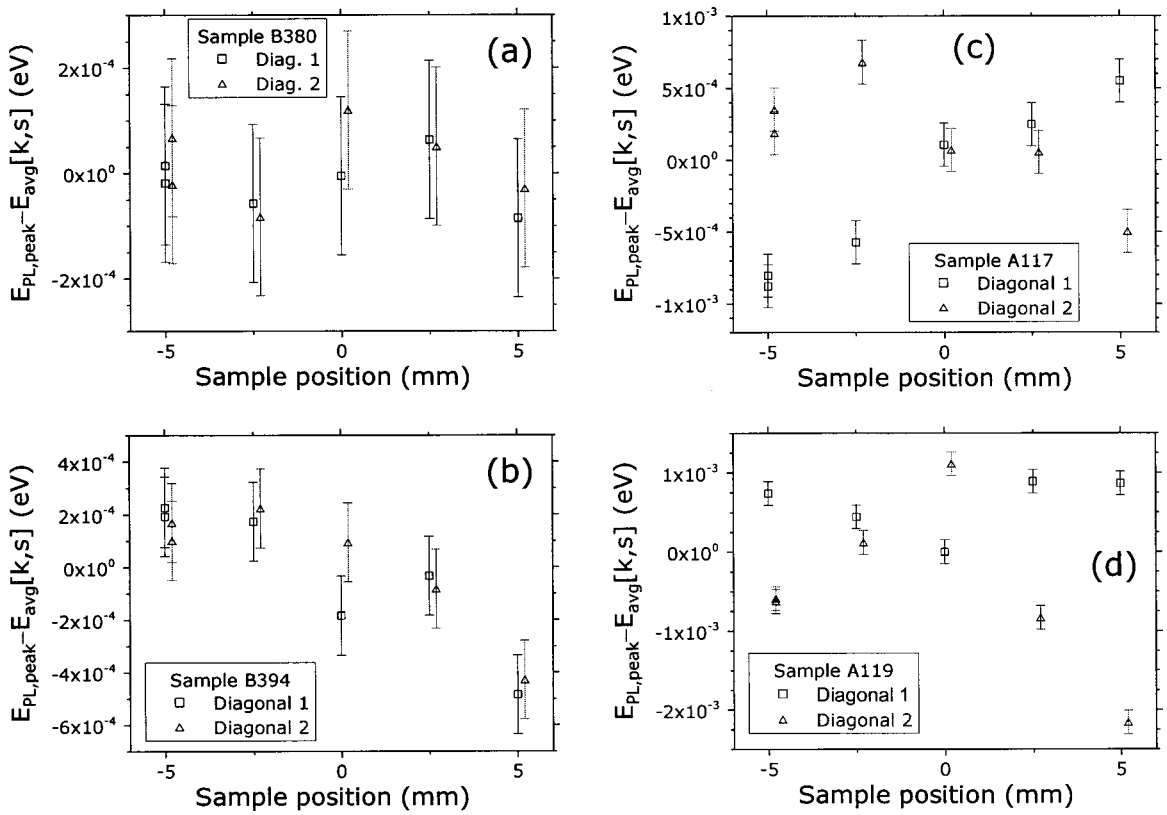

FIG. 7. Measured spatial variation of $\mathbf{E}_{PL,peak}$ for five samples (following the "test pattern" shown in Fig. 1). For clarity, diagonal 2 locations are plotted with an arbitrary horizontal offset from diagonal 1 locations. Note that the plotted *y*-axis (photon energy) range is different for each sample; (a) sample B309; with $\mathbf{x}_{WDS}=0.2200$, (b) sample B380; with $\mathbf{x}_{WDS}=0.2010$, (c) sample B394; with $\mathbf{x}_{WDS}=0.2775$, (d) sample A117; with $\mathbf{x}_{WDS}=0.1908$, and (e) sample A119; with $\mathbf{x}_{WDS}=0.2008$.

The discrepancy between the RHEED and WDS results for sample B309, and inconsistencies between different RHEED measurements of A128 (this sample was not examined by WDS), provided further evidence for inhomogeneity in these two samples. In addition, one of the A reactor samples (A121) and three of the B reactor samples (B274, B373, and B379) were excluded for high carrier concentration, which caused a noticeable shift of $\mathbf{E}_{PL,peak}$. The carrier concentration effect will be discussed in more detail later. A plot of PL energy, $\mathbf{E}_{PL,peak}$, versus WDS composition, $\mathbf{x}_{WDS}$, as well as the best linear fit to the data, is shown in Fig. 8. The data points are seen to follow a linear ralation to good accuracy. The equation of the best-fit line is

$$\mathbf{E}_{PL,peak}=(1.4017\pm0.00900\ \text{eV})\mathbf{x}_{WDS}+1.423\,26 \pm0.000\,47\ \text{eV}. \tag{11}$$

The inverse equation, which can be used to predict the composition as a function of PL peak energy, is

$$\mathbf{x}_{\{PL|WDS\}}=(0.7134\pm0.0046\ \text{eV}^{-1})(\mathbf{E}_{PL,peak}-1.423\,26 \pm0.000\,47\ \text{eV}). \tag{12}$$

The notation $\mathbf{x}_{\{PL|WDS\}}$ is used to indicate a value derived from correlating the measured values of $\mathbf{E}_{PL,peak}$ and $\mathbf{x}_{WDS}$. In other words, $\mathbf{x}$ can be determined from the PL data only after the PL results are calibrated against a direct composition measurement method.

By combining Eq. (11) with Eq. (1) (that gives the temperature coefficient of $\mathbf{E}_{PL,peak}$), an expression for both the temperature and composition dependence of $\mathbf{E}_{PL,peak}$ is obtained:

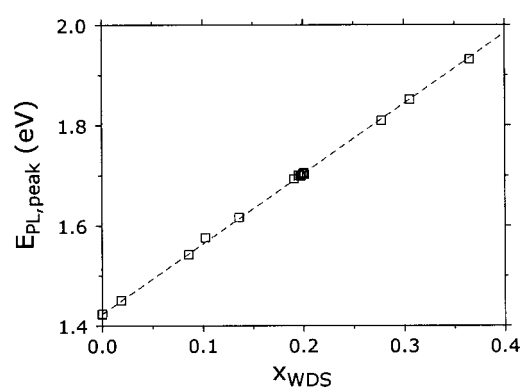

FIG. 8. Linear correlation between PL peak energy, $\mathbf{E}_{PL,peak}$, and WDS composition, $\mathbf{x}_{WDS}$ for calibration set of one GaAs film and fourteen $Al_xGa_{1-x}As$ films. Data points are shown as squares, and the best linear fit to the data is shown as a dashed line. The uncertainty of $\mathbf{E}_{PL,peak}$ for most samples shown in this plot, taking into account long-term temperature drift and spatial nonuniformity, is of the order 5×10^{-4} eV; error bars are not shown because of the small magnitude of the uncertainties relative to the plot scale.

Downloaded 17 Feb 2005 to 132.163.53.137. Redistribution subject to AIP license or copyright, see http://jap.aip.org/jap/copyright.jsp

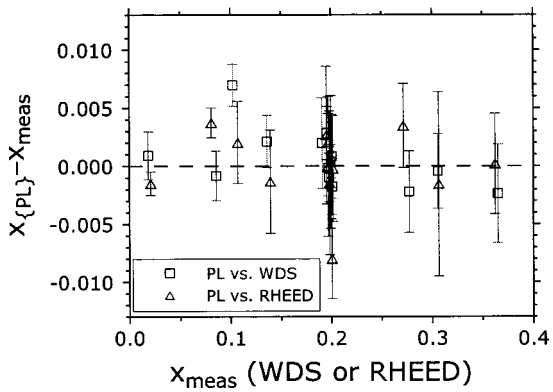

FIG. 9. Deviation between fitted PL composition and measured composition, $\mathbf{x}_{\{PL|WDS\}}-\mathbf{x}_{WDS}$ or $\mathbf{x}_{\{PL|RHEED\}}-\mathbf{x}_{RHEED}$, plotted as a function of measured composition, $\mathbf{x}_{WDS}$ or $\mathbf{x}_{RHEED}$. Data for {PL|WDS} fit are shown as squares, data for {PL|RHEED} fit are shown as triangles.

$$\begin{aligned}\mathbf{E}_{PL,peak}=&\{1.4017\pm0.0090\ \text{eV}-(2.71\pm0.97)\\&\times10^{-4}(\text{eV/K})(\mathbf{T}_{exc}-298.3\ \text{K})\}\mathbf{x}_{WDS}\\&+1.423\,26\pm0.000\,47\ \text{eV}-(4.74\pm0.23)\\&\times10^{-4}(\text{eV/K})(\mathbf{T}_{exc}-298.3\ \text{K})\\&+((1.05\pm0.16)\times10^{-10}-(0.29\pm0.11)\\&\times10^{-10}\,\text{sgn}[\mathbf{n}])|\mathbf{n}|^{1/3}(\mathbf{T}_{exc}-298.3\ \text{K}).\end{aligned}\tag{13}$$

As discussed, $\mathbf{T}_{exc}$ is the actual temperature of the PL excitation volume, and $\mathbf{T}_{exc}=298.3$ K is the value of this temperature with the standard experimental conditions used in the present study. Equation (13) can thus be used to calculate PL-composition calibration curves at other temperatures near "room temperature."

When $\mathbf{E}_{PL,peak}$ is correlated with $\mathbf{x}_{RHEED}$ rather than $\mathbf{x}_{WDS}$, the slope of the best-fit line [analogous to Eq. (11)] is found to be $\partial\mathbf{E}_{PL,peak}/\partial\mathbf{x}_{RHEED}=1.4021\pm0.0106$ eV, and the inverse slope [analogous to Eq. (12)] is $\partial\mathbf{x}_{\{PL|RHEED\}}/\partial\mathbf{E}_{PL,peak}=0.7132\pm0.0054\ \text{eV}^{-1}$. The difference between $\partial\mathbf{E}_{PL,peak}/\partial\mathbf{x}_{WDS}$ and $\partial\mathbf{E}_{PL,peak}/\partial\mathbf{x}_{RHEED}$ is 4×10^{-4} eV, much smaller than the uncertainty of either slope. The close agreement between the fitted values of $\partial\mathbf{E}_{PL,peak}/\partial\mathbf{x}_{WDS}$ and $\partial\mathbf{E}_{PL,peak}/\partial\mathbf{x}_{RHEED}$ (better than expected from the error analysis) may be fortuitous.

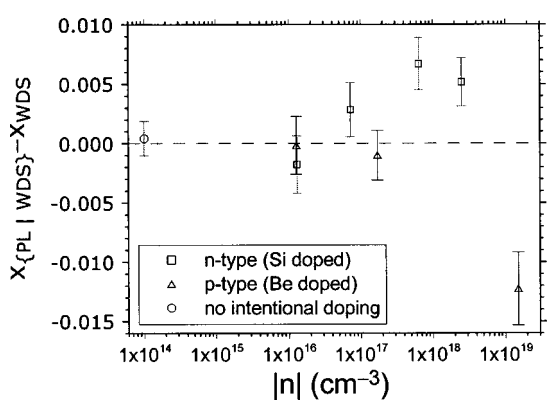

FIG. 10. Effect of *n*- and *p*-type doping on nominal, fitted PL composition, $\mathbf{x}_{\{PL|WDS\}}$. The difference $\mathbf{x}_{\{PL|WDS\}}-\mathbf{x}_{WDS}$ is plotted as a function of the absolute value of the carrier concentration, $|\mathbf{n}|$, for samples with compositions near $\mathbf{x}_{WDS}=0.2$ and varying carrier concentrations. In the plot, *n*-type samples are represented by squares, *p*-type samples are represented by triangles, and an undoped sample (with carrier concentration too small to measure, assumed to be 10^{14} cm^{-3}) is represented by a circle.

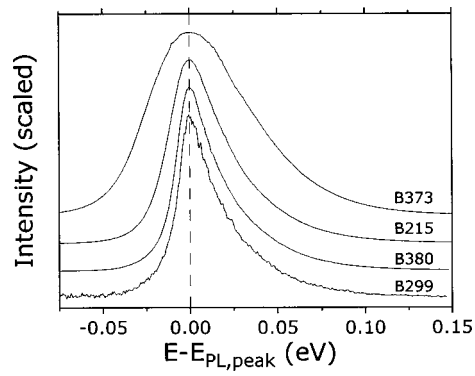

FIG. 11. Room-temperature PL spectra from four undoped or *n*-type samples with $\mathbf{x}_{WDS}\approx0.2$: B299 (undoped), B380 ($|\mathbf{n}|=1.3\times10^{16}$ cm^{-3}), B215 ($|\mathbf{n}|=7.2\times10^{16}$ cm^{-3}), and B373 ($|\mathbf{n}|=6.4\times10^{17}$ cm^{-3}). To simplify comparison of the line shapes, the energy scale for each spectrum is set to $\mathbf{E}-\mathbf{E}_{PL,peak}$, the peak intensity of each spectrum is rescaled to unity, and spectra are offset vertically. The peak energy ($\mathbf{E}=\mathbf{E}_{PL,peak}$) is indicated by a vertical dashed line.

Table I lists the values of several important parameters for all of the examined films: column 1, sample name; column 2, PL peak energy and measurement uncertainty $\mathbf{E}_{PL,peak}[s]\pm2\sigma_{E,total}[s]$; column 3, WDS composition and measurement uncertainty, $\mathbf{x}_{WDS}[s]\pm2\sigma_x[s]$; column 4, RHEED composition and measurement uncertainty, $\mathbf{x}_{RHEED}[s]\pm2\sigma_x[s]$; column 5, fitted {PL|WDS} composition from Eq. (12) and calculated uncertainty, $\mathbf{x}_{\{PL|WDS\}}[s]\pm2\sigma_x[s]$; column 6, the contribution to the uncertainty of $\mathbf{x}_{\{PL|WDS\}}[s]$ from the PL peak energy uncertainties of the sample ($\mathbf{E}_{PL,peak}[s]\pm2\sigma_{E,total}[s]$) and the $x=0$ (GaAs) reference point ($1.423\,26\pm0.000\,47$ eV); and finally column 7, the contribution to the uncertainty of $\mathbf{x}_{\{PL|WDS\}}[s]$ from the uncertainty in the slope ($\partial\mathbf{x}_{WDS}/\partial\mathbf{E}_{PL,peak}=0.7134\pm0.0046\ \text{eV}^{-1}$). The two components of the uncertainty of $\mathbf{x}_{\{PL|WDS\}}[s]$ are listed separately because they originate from different measurements. The uncertainties in the PL peak energies arise only from the PL measurements, whereas the slope uncertainty arises primarily from the WDS measurements. The magnitude of the first uncertainty component (column 6) is similar for most samples, while the magnitude of the second component (column 7) increases with increasing $\mathbf{x}$.

In Fig. 9, the differences between the fitted {PL|WDS} compositions from Eq. (12) and the measured WDS compositions, $\mathbf{x}_{\{PL|WDS\}}[s]-\mathbf{x}_{WDS}[s]$, are plotted as a function of $\mathbf{x}_{WDS}$ (squares). The error bars shown for $\mathbf{x}_{\{PL|WDS\}}[s]-\mathbf{x}_{WDS}[s]$ in Fig. 9 are the quadrature sum of the uncertainties of $\mathbf{x}_{WDS}$ (from the third column of Table I) and $\mathbf{x}_{\{PL|WDS\}}$ (from the fifth column of Table I). In addition, the differences between the fitted {PL|RHEED} compositions and the measured RHEED compositions, $\mathbf{x}_{\{PL|RHEED\}}[s]-\mathbf{x}_{RHEED}[s]$, are plotted as a function of $\mathbf{x}_{RHEED}$ (squares). The error bars shown for $\mathbf{x}_{\{PL|RHEED\}}[s]-\mathbf{x}_{RHEED}[s]$ are the

Downloaded 17 Feb 2005 to 132.163.53.137. Redistribution subject to AIP license or copyright, see http://jap.aip.org/jap/copyright.jsp

TABLE II. Polynomial coefficients of function $\mathbf{E}_G[\mathbf{x}]$, where $\mathbf{E}_G$ is the optical band gap of $Al_xGa_{1-x}As$ (determined by PL or another spectroscopic technique) and $\mathbf{x}$ is the Al fraction, as reported in the present study and previous studies. Coefficients are in eV units.

Publication	Constant term (GaAs band gap)	Constant term (corrected, 298 K)	Linear term	Linear term (corrected, 298 K)	Quadratic term	Cubic term
Present study	1.4233	1.4233	1.402	1.402	0	0
Casey and Panish (1978)	1.424	1.424	1.247	1.247	0	0
Miller (1985)	1.42	1.42	1.45	1.45	−0.25	0
Aspnes (1986)	1.424	1.424	1.721	1.721	−1.437	1.310
Kuech (1987)	1.512	1.420	1.455	1.402	0	0
Lambert (1987)	not reported	not reported	1.287	1.234	0	0
Oelgart (1987)	1.425	1.425	1.35	1.35	0	0
Bosio (1988)	1.5152	1.4232	1.480	1.427	0	0
Huang (1988)	1.424	1.424	1.427	1.427	0.041	0
Wasilewski (1999)	1.515	1.423	1.403	1.350	0	0

quadrature sum of the uncertainties of $\mathbf{x}_{\mathrm{RHEED}}$ (from the fourth column of Table I) and $\mathbf{x}_{\{\mathrm{PL}|\mathrm{RHEED}\}}$ (not shown in Table I). The typical magnitude of the difference between the fitted line and the data is seen to be similar for the {PL|WDS} and {PL|RHEED} regressions.

H. Impurity doping effects

The effect of *n*- and *p*-type doping on the nominal PL composition, $\mathbf{x}_{\{\mathrm{PL}|\mathrm{WDS}\}}$ from Eq. (12), is shown in Fig. 10, where the difference $\mathbf{x}_{\{\mathrm{PL}|\mathrm{WDS}\}}[s]-\mathbf{x}_{\mathrm{WDS}}[s]$ is plotted as a function of carrier concentration for samples with $\mathbf{x}_{\mathrm{WDS}} \approx 0.2$ and varying doping levels. The carrier concentration of the sample with no intentional doping was too small to measure; a carrier concentration of 10^{14} cm^{-3} is assumed for this sample. The error bars shown for $\mathbf{x}_{\{\mathrm{PL}|\mathrm{WDS}\}}[s]-\mathbf{x}_{\mathrm{WDS}}[s]$ in Fig. 10 are the quadrature sum of the uncertainties of $\mathbf{x}_{\mathrm{WDS}}$ (from the third column of Table I) and $\mathbf{x}_{\{\mathrm{PL}|\mathrm{WDS}\}}$ (from the fifth column of Table I). The difference $\mathbf{x}_{\{\mathrm{PL}|\mathrm{WDS}\}}[s]-\mathbf{x}_{\mathrm{WDS}}[s]$ is seen to become positive for heavy *n*-type doping and negative for heavy *p*-type doping; in other words, the PL peak energy shifts upward for heavy *n*-type doping, and downward for heavy *p*-type doping. Samples with *n*-type carrier concentration $|\mathbf{n}|>10^{17}$ cm^{-3}, or *p*-type carrier concentration $|\mathbf{n}|>2\times10^{17}$ cm^{-3} were thus excluded from the PL-composition calibration set. Figure 10 indicates that carrier concentrations up to these limits are acceptable for PL-composition measurements with an uncertainty of ±0.003 in the value of $\mathbf{x}$. If a smaller uncertainty were specified, then further examination of the doping effects would be necessary.

The full width at half maximum (FWHM) of the PL spectrum increases with increasing carrier concentration. Further, the curvature (or "sharpness") of the peak shows a decrease with increasing carrier concentration, starting at concentrations as low as $\approx10^{16}$ cm^{-3}, which is proportionally larger than the increase of the FWHM. In Fig. 11, PL spectra from four samples with $\mathbf{x}_{\mathrm{WDS}}\approx0.2$ are compared: B299 (undoped), B380 ($|\mathbf{n}|=1.3\times10^{16}$ cm^{-3}), B215 ($|\mathbf{n}|=7.2\times10^{16}$ cm^{-3}), and B373 ($|\mathbf{n}|=6.4\times10^{17}$ cm^{-3}). The energy scale for each spectrum is $\mathbf{E}-\mathbf{E}_{\mathrm{PL,peak}}[s]$ (i.e., the spectra are shifted horizontally to align the peaks), and the peak intensities are rescaled to unity. The decrease in the peak sharpness causes the measurement uncertainty of $\mathbf{E}_{\mathrm{PL,peak}}$ to increase in the more heavily doped samples. The fixed location, single-run uncertainty of $\mathbf{E}_{\mathrm{PL,peak}}$ (as defined herein) is $\approx1.2\times10^{-3}$ eV for sample B373, as compared to $\approx1.5\times10^{-4}$ eV for the low carrier concentration samples.

The high sharpness of the PL peak at low carrier concentrations can be explained by a recombination model proposed by Grilli *et al.*[15] and Venu Gopal *et al.*[16] in PL temperature dependence studies of high-purity GaAs. According to this model, the observed band-edge PL spectrum is a sum of two bell-shaped peaks with similar peak intensities but differing linewidths, corresponding to distinct recombination processes: A relatively narrow excitonic peak (present even at room temperature), and a much broader free-electron-to-free-hole peak. The peak energy of the summed line is thus "pulled" toward the relatively narrow excitonic peak, although the integrated intensity is dominated by the broader free-to-free peak.

We suggest that the Grilli[15] and Venu Gopal[16] model is applicable to the lower carrier concentration samples in our study, and that the measured $\mathbf{E}_{\mathrm{PL,peak}}$ values of these samples are mainly determined by the excitonic component. We did not try to deconvolute the excitonic and free-to-free components of the PL spectrum in the curve-fitting procedure (see

Downloaded 17 Feb 2005 to 132.163.53.137. Redistribution subject to AIP license or copyright, see http://jap.aip.org/jap/copyright.jsp

TABLE III. Measurement methods used to determine function $\mathbf{E}_G[\mathbf{x}]$, where $\mathbf{E}_G$ is the optical band gap of $Al_xGa_{1-x}As$ (determined by PL or another spectroscopic technique) and $\mathbf{x}$ is the Al mole fraction, for present study and previous studies.

Publication	Measurement method for $\mathbf{x}$	Measurement method for $\mathbf{E}_G$	Measurement temperature for $\mathbf{E}_G$
Present study	WDS/EMPA (checked by *in situ* RHEED)	PL spectroscopy, peak energy from curve fitting	298 K
Casey and Panish (1978) (curve A)	EMPA (composite of earlier studies)	PL peak energy (composite of earlier studies)	297 K
Miller (1985) (curve B)	EMPA (with standards including AlCu alloy)	PL peak energy	"room"
Aspnes (1986) (curve C)	"target" composition in LPE deposition system	spectroscopic ellipsometry	room
Kuech (1987) (curve D)	NRRA	PL peak energy	2 K
Lambert (1987) (curve E)	x-ray diffraction, 004 peak rocking curves	PL peak energy	2 K
Oelgart (1987) (curve F)	EMPA	PL peak energy	300 K
Bosio (1988) (curve G)	EMPA	Transmittance spectroscopy (exciton absorption peak)	2 K
Huang (1988) (curve H)	NRRA	Photoreflectance	room
Wasilewski (1999) (curve I)	Al and Ga atomic arrival rates determined from x-ray diffraction of multilayer "calibration" structures	PL peak energy	8 K

Appendix), as this would have significantly increased the complexity of the model function.

I. Comparison with previous results

In this section, the composition dependence of the PL peak energy given by Eqs. (11) and (13) is compared with results previously reported[2–10] in the literature for the composition dependence of the $Al_{1-x}Ga_xAs$ band gap energy, as measured by PL or other spectroscopic techniques such as transmittance or photoreflectance.

Some of the previous measurements were done with the sample at low temperature ($\mathbf{T} \leqslant 10$ K), while the present study and other previous measurements were done at room temperature ($\mathbf{T} = 298.3$ K in the present study). A temperature correction term was added to the low-temperature results to assist with comparison to the room-temperature results. The temperature correction term was calculated by first extrapolating Eq. (13) from $\mathbf{T} = 298.3$ K to $\mathbf{T} = 0$ K, and then multiplying the resulting equation by a factor of 0.65 to obtain the correct temperature shift of $\Delta\mathbf{E}_{PL,peak}[0 \rightarrow 298.3\ \mathrm{K}] = -0.0920 \pm 0.0005$ eV for pure GaAs. [The factor of 0.65 accounts for the decrease of the magnitude of the temperature coefficient of $\mathbf{E}_{PL,peak}$ with decreasing temperature, due to freeze out of the lattice thermal expansion. $\mathbf{E}_{PL,peak}$ for pure GaAs is equal to 1.5153 ± 0.0002 eV at low temperature (free exciton, from Ref. 15) and to 1.4233 ± 0.0005 eV at 298.3 K (from Table I).] The resulting low-temperature to room-temperature correction is

$$\Delta\mathbf{E}_{PL,peak}[0 \rightarrow 298.3\ \mathrm{K}] = -0.0920 \pm 0.0005\ \mathrm{eV} - (0.0526 \pm 0.0190\ \mathrm{eV})\mathbf{x}. \quad (14)$$

Table II lists the polynomial coefficients (up to third or-

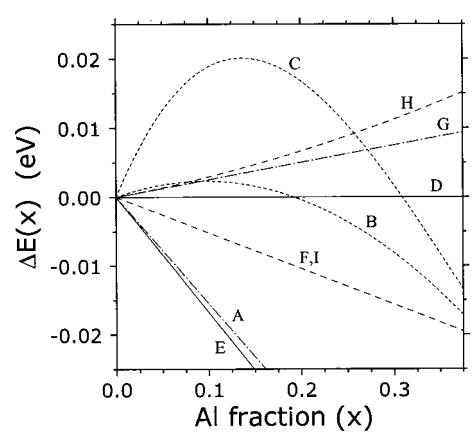

FIG. 12. Differences between the composition-dependent ($\mathbf{x} > 0$) parts of the functions $\mathbf{E}_G[\mathbf{x}]$ determined in previous studies, and in the present study, where $\mathbf{E}_G$ is the optical band gap of $Al_xGa_{1-x}As$ (determined by PL or another spectroscopic technique) and $\mathbf{x}$ is the Al fraction. [Curve A: Casey and Panish (1978) (see Ref. 2). Curve B: Miller (1985) (see Ref. 3). Curve C: Aspnes (1986) (see Ref. 4). Curve D: Kuech (1987) (see Ref. 5). Curve E: Lambert (1987) (see Ref. 6). Curve F: Oelgart (1987) (see Ref. 7). Curve G: Bosio (1988) (see Ref. 8). Curve H: Huang (1988) (see Ref. 9). Curve I: Wasilewski (1997) (see Ref. 10).] Note that a correction term for the composition-dependent part of the temperature shift between low temperature and room temperature was added to the low-temperature results (curves D, E, G, and I) to assist with comparison to the room-temperature results.

Downloaded 17 Feb 2005 to 132.163.53.137. Redistribution subject to AIP license or copyright, see http://jap.aip.org/jap/copyright.jsp

der) of the function $\mathbf{E}_G[\mathbf{x}]$, as reported in each of the previous[2–10] studies, as well as the present study. (The notation $\mathbf{E}_G[\mathbf{x}]$ is used here, rather than $\mathbf{E}_{\mathrm{PL,peak}}[\mathbf{x}]$, because some of the previous studies used other optical spectroscopy methods, such as transmittance or photoreflectance, to measure the band gap.) The low-temperature to room-temperature correction term [Eq. (14)] was added as required. Table III summarizes the experimental methods used to measure the composition and band gap energy in each of the previous studies and the present study. The differences between the functions $\mathbf{E}_G[\mathbf{x}]$ determined in each of the previous studies, and the present study, are plotted in Fig. 12. To generate this plot, the functions were offset slightly to align the values of $\mathbf{E}_G[\mathbf{x}=0]$ (GaAs band gap). The curve identification symbols from Fig. 12 (curve A, curve B, etc.) are repeated in Table III for convenience.

Further adjustments were made to the coefficients of $\mathbf{E}_G[\mathbf{x}]$ reported in two previous studies to provide a more consistent comparison between studies. Lambert *et al.*[6] (curve E) added an exciton binding energy term to their PL data, to obtain the free-electron-to-free-hole band gap, whereas we and most other researchers used the PL peak energy (or other spectroscopically measured energy), and did not try to correct for the exciton binding energy. To eliminate this discrepancy, we examined the composition dependence of the actual $\mathbf{E}_{\mathrm{PL,peak}}$ values reported by Lambert *et al.*[6] without their exciton binding energy correction. Bosio *et al.*[8] (curve G) stated that their low-temperature $\mathbf{E}[\mathbf{x}]$ data are fit very well by a straight line with a slope of 1.48 eV, but then adjusted their fit by adding a quadratic term in order to match the direct band gap of AlAs previously reported by Monemar[17] ($\mathbf{E}_G=3.13$ eV at $\mathbf{x}=1$). If this adjustment were accepted, then, for consistency, it would be necessary to make similar adjustments to all the other fits to match the AlAs band gap reported by Monemar.[17] In Table II and Fig. 12, the empirical linear fit to the data of Bosio *et al.*[8] is thus used rather than the adjusted quadratic fit.

Inspection of Fig. 12 shows that some of the previously determined $\mathbf{E}_G[\mathbf{x}]$ calibration curves differ significantly from the present result and from each other. The origins of the measurement errors (in $\mathbf{x}$ or $\mathbf{E}_G$) that give rise to these deviations are not known. It is possible, however, to speculate about the sources of error in the curves that show the largest deviation from the present result, namely curves A, C, and E (a difference of greater than 0.02 eV in the predicted value of $\mathbf{E}_G[\mathbf{x}]$ for compositions $\mathbf{x}<0.2$). Curve A is derived from WDS/EMPA measurements and analyses done in the time period 1969 to 1971 (see Ref. 2), significantly earlier than the other studies; the WDS correction algorithms (used to obtain the chemical composition from the measured WDS/EMPA spectra) available at that time are believed to be less accurate than later-developed WDS correction algorithms. The composition for curve C was estimated from the concentrations of the source materials in a liquid-phase epitaxy (LPE) system, and is thus susceptible to errors in modeling of the crystal growth chemistry (Al/Ga incorporation ratio). The composition for curve E is derived from x-ray rocking curve measurements, with the assumption that the lattice constant is an accurately linear function of composition (Vegard's law); later studies have shown that Vegard's law does not hold[18,19] in the $\mathrm{Al}_x\mathrm{Ga}_{1-x}\mathrm{As}$ system.

The low-temperature results of Kuech (curve D), based on NRRA of the composition, match the results of the present study within experimental error after applying the low-temperature to room-temperature correction, Eq. (15) in the Appendix. The room-temperature results of Huang (curve H), also based on nuclear resonant reaction analysis, show a small but measurable difference from Kuech (curve D) and the present study; the source of this discrepancy is not known.

IV. CONCLUSIONS

The room-temperature PL peak emission energy, $\mathbf{E}_{\mathrm{PL,peak}}$ was measured for a set of MBE-grown $\mathrm{Al}_x\mathrm{Ga}_{1-x}\mathrm{As}$ films with Al mole fraction $0\leqslant\mathbf{x}<0.37$, and correlated with alloy composition as determined by *in situ* RHEED and *ex situ* WDS/EMPA. The measurement uncertainty (2σ level) of $\mathbf{E}_{\mathrm{PL,peak}}$ was of the order $\pm5\times10^{-4}$ eV for most films, much smaller than the peak FWHM of 0.03 eV. Long-term fluctuations in the temperature sensor readout (used to compensate for ambient temperature variation), run-to-run variations in the temperature gradient between the temperature sensor and the sample volume probed by PL, and composition gradients as a function of location on the film, are believed to make major contributions to the uncertainty. Thus, with better sample temperature control and more homogeneous composition, the uncertainty of $\mathbf{E}_{\mathrm{PL,peak}}$ could be reduced further. From correlation of the PL and WDS/EMPA data, the slope of the $\mathbf{E}_{\mathrm{PL,peak}}$ versus composition curve near room temperature was determined to be $\partial\mathbf{E}_{\mathrm{PL,peak}}/\partial\mathbf{x}=(1.4017\pm0.0090\ \mathrm{eV})-((2.71\pm0.97)\times10^{-4}\ \mathrm{eV/K})(\mathbf{T}-298.3\ \mathrm{K})$. Correlation of the PL and RHEED data yielded a value of $\partial\mathbf{E}_{\mathrm{PL,peak}}/\partial\mathbf{x}$ which is indistinguishable within experimental error from the aforementioned value. Previously published measurements of $\partial\mathbf{E}_{\mathrm{PL,peak}}/\partial\mathbf{x}$ were compared with the present study. The results of Kuech *et al.*,[5] which are based on nuclear resonant reaction analysis of the Al mole fraction, are in good agreement with the present study after addition of a correction term to account for the effect of sample temperature on $\partial\mathbf{E}_{\mathrm{PL,peak}}/\partial\mathbf{x}$ ($\mathbf{T}=2$ K for Kuech,[5] $\mathbf{T}=298$ K for the present study). Some reasons are suggested for the large variation in the values of $\partial\mathbf{E}_{\mathrm{PL,peak}}/\partial\mathbf{x}$ reported in the previous studies.

APPENDIX

From inspection (Fig. 2), the PL line shape is described as an asymmetric, single-peaked, bell-shaped curve, skewed toward the high-energy side. When the spectral data are plotted on a semilogarithmic scale, as in the inset to Fig. 2(b), both the high- and low-energy tails are seen to have exponential forms. A function $\mathbf{I}_{\mathrm{PL}}[\mathbf{E}]$ with five adjustable parameters ($\mathbf{E}_{\mathrm{PL,peak}}$, $\mathbf{I}_{\mathrm{max}}$, $\mathbf{W}$, $\mathbf{P}$, and σ) that meets all the aforementioned criteria is defined by

Downloaded 17 Feb 2005 to 132.163.53.137. Redistribution subject to AIP license or copyright, see http://jap.aip.org/jap/copyright.jsp

$$\begin{aligned}
&\mathbf{I}_{\mathrm{PL}}[\mathbf{E}]=\mathbf{I}_{\max}(\mathrm{sech}[\mathbf{Q}\mathbf{Z}_1])^{\mathbf{P}},\\
&\mathbf{Z}_1=\mathbf{Z}_0/(1-\sigma)\quad \text{for}\quad \mathbf{E}<\mathbf{E}_{\mathrm{PL,peak}},\\
&\mathbf{Z}_1=\mathbf{Z}_0/(1+\sigma)\quad \text{for}\quad \mathbf{E}>\mathbf{E}_{\mathrm{PL,peak}},\\
&\mathbf{Z}_0=(2/\mathbf{W})*(\mathbf{E}-\mathbf{E}_{\mathrm{PL,peak}}),\\
&\mathbf{Q}=(\ln[2]/\mathbf{P})+\ln[1+(1-2^{(-2/\mathbf{P})})^{0.5}],
\end{aligned}\tag{15}$$

where $\mathbf{E}$ is the photon energy, $\mathbf{I}_{\mathrm{PL}}$ is the PL intensity, $\mathbf{E}_{\mathrm{PL,peak}}$ is the energy at the peak of the line, $\mathbf{I}_{\max}$ is the intensity at the peak, $\mathbf{W}$ is the FWHM, the parameter $\mathbf{P}$ is correlated with the ratio of the curvature at the peak to the full width (note the variation of this ratio in the spectra plotted in Fig. 11), and σ is a skewing or asymmetry parameter. The half width at half maximum is $\mathbf{W}(1+\sigma)/2$ on the high-energy side of the peak, and $\mathbf{W}(1-\sigma)/2$ on the low-energy side. This function is similar to the ''split Pearson VII'' function[20] sometimes used to fit x-ray diffraction peaks, but with exponential rather than power-law tails.

The five-parameter ''split asymmetric'' function of Eq. (15) is discontinuous in its second and higher derivatives at $\mathbf{E}=\mathbf{E}_{\mathrm{PL,peak}}$. Another dimensionless parameter, τ, described as the ''asymmetry transition width,'' is introduced to remove the discontinuity. A ''smoothed asymmetric'' function with six adjustable parameters ($\mathbf{E}_{\mathrm{PL,peak}}$, $\mathbf{I}_{\max}$, $\mathbf{W}$, $\mathbf{P}$, σ, τ) is defined by

$$\begin{aligned}
&\mathbf{I}_{\mathrm{PL}}[\mathbf{E}]=\mathbf{I}_{\max}(\mathrm{sech}[\mathbf{Q}\mathbf{Z}_1])^{\mathbf{P}},\\
&\mathbf{Z}_1\{1+\sigma\tanh[\mathbf{Z}_1/\tau]\}=\mathbf{Z}_0
\end{aligned}\tag{16}$$

with the same definitions of $\mathbf{Z}_0$ and $\mathbf{Q}$ as in Eq. (15). Note that the smoothed asymmetric function, Eq. (16), reduces to the split asymmetric function, Eq. (15), in the limit $\tau\rightarrow 0$. Significantly better fits to the measured PL spectra were obtained with Eq. (16) than with Eq. (15). Therefore, the curve-fitting analysis of the measured spectra was based on the smoothed asymmetric function, Eq. (16).

[1] T. E. Gills, S. Dittman, J. R. Rumble, C. S. Brickenkamp, G. L. Harris, and N. M. Trahey, J. Res. Natl. Inst. Stand. Technol. **106**, 315 (2001).
[2] H. C. Casey and M. B. Panish, *Heterostructure Lasers* (Academic, New York, 1978), pp. 191–194.
[3] N. C. Miller, S. Zemon, G. P. Werber, and W. Powaznik, J. Appl. Phys. **57**, 512 (1985).
[4] D. E. Aspnes, S. M. Kelso, R. A. Logan, and R. Bhat, J. Appl. Phys. **60**, 754 (1986).
[5] T. F. Kuech, D. J. Wolford, R. Potemski, J. A. Bradley, K. H. Kelleher, D. Yan, J. P. Farrell, P. M. S. Lesser, and F. H. Pollak, Appl. Phys. Lett. **51**, 505 (1987).
[6] B. Lambert, J. Caulet, A. Regreny, M. Baudet, and B. Deveaud, Semicond. Sci. Technol. **2**, 491 (1987).
[7] G. Oelgart, R. Schwabe, M. Heider, and B. Jacobs, Semicond. Sci. Technol. **2**, 468 (1987).
[8] C. Bosio, J. L. Staehli, M. Guzzi, G. Burri, and R. A. Logan, Phys. Rev. B **38**, 3263 (1988).
[9] D. Huang, G. Ji, U. K. Reddy, H. Morkoc, F. Xiong, and T. A. Tombrello, J. Appl. Phys. **63**, 5447 (1988).
[10] Z. R. Wasilewski, M. M. Dion, D. J. Lockwood, P. Poole, R. W. Streater, and A. J. SpringThorpe, J. Appl. Phys. **81**, 1683 (1997).
[11] C. E. C. Wood, in *The Technology and Physics of Molecular-beam Epitaxy*, edited by E. H. C. Parker (Plenum, New York, 1985), p. 67.
[12] Reference to specific products or trade names does not constitute an endorsement by the National Institute of Standards and Technology. Other vendors may provide products of comparable or superior value.
[13] P. Lautenschlager, M. Garriga, S. Logothetidis, and M. Cardona, Phys. Rev. B **35**, 9174 (1986).
[14] S. Logothetidis, M. Cardona, and M. Garriga, Phys. Rev. B **43**, 11950 (1991).
[15] E. Grilli, M. Guzzi, R. Zamboni, and L. Pavesi, Phys. Rev. B **45**, 1638 (1992).
[16] A. Venu Gopal, R. Kumar, A. S. Vengurlekar, A. Bosacchi, S. Franchi, and L. N. Pfeiffer, J. Appl. Phys. **87**, 1858 (2000).
[17] B. Monemar, Phys. Rev. B **8**, 5711 (1973).
[18] Z. R. Wasilewski, M. M. Dion, D. J. Lockwood, P. Poole, R. W. Streater, and A. J. SpringThorpe, J. Appl. Phys. **81**, 1683 (1997).
[19] D. Zhou and B. F. Usher, J. Phys. D **34**, 1461 (2001).
[20] M. Oetzel and G. Heger, J. Appl. Crystallogr. **32**, 799 (1999).

Downloaded 17 Feb 2005 to 132.163.53.137. Redistribution subject to AIP license or copyright, see http://jap.aip.org/jap/copyright.jsp